Transparent Metals for Ultrabroadband Electromagnetic Waves

Ren-Hao Fan, Ru-Wen Peng, Xian-Rong Huang,* Jia Li, Yongmin Liu, Qing Hu, Mu Wang,* and Xiang Zhang*

Bulk metals, such as gold, silver and copper, are all naturally opaque to light due to the large mismatch of refractive index between the metals and dielectrics. Making metals transparent, which could lead to various fascinating applications, has long been pursued. Recently by developing structured materials, it is possible to design the electromagnetic properties of materials beyond the nature. For example, in the structured metals, the excited free electrons may induce surface plasmons (SPs)[1] or spoof surface plasmons (SSPs) in the long-wavelength regime,[2] which are essentially the collective surface charge density waves and propagate along slit or hole walls, nanowires, channels, etc. When the propagation is terminated by the geometric boundaries, SPs can be converted back into light, contributing to extraordinary transmission of light through the structured metals.[3–10] Besides, engineered metallic structures have been used as building blocks[11] to construct metamaterials,[12] which offer the possibilities for superlenses,[13] negative refractive indices,[14] high indices of refraction,[15] and many other fanscinating phenomena and applications. However, these artificial structures have some common drawbacks. One is the narrow transmission bandwidths that typically appear as discrete resonant peaks, which allows the device working only at several specific frequencies. The other is the low transmission efficiency for thick materials. Nowadays, people are struggling to expand the working bandwidth and increase the transmission efficiency for applications. For example, both Huang et al.[6] and Alu et al.[7] proposed that metallic gratings consisting of narrow slits can become transparent for extremely broad bandwidths under oblique incidence, which is associated with the excitation of SPs (or SSPs). Recently, Subramania et al.[8] theoretically studied broadband funneling of light via ultrasubwavelength channels, and such channels significantly create non-resonant metallic platform possessing broadband transparency features. Nevertheless, no experimental work has been conducted so far to make metal panels highly transparent and antireflective, particularly for white light.

In this communication, we demonstrate for the first time with experiments that metallic gratings consisting of narrow slits can become non-dispersively transparent for terahertz (THz) waves. The broadband optical transmission is verified for the structured metals with thickness within the range of half a wavelength, and the high transmission efficiency is in fact insensitive to the metal thickness. Furthermore, this approach can implement transparent metals nearly over the entire spectrum ranging from the radio frequency to the visible. The investigations provide a guideline to develop many novel devices, including transparent conducting panels, white-beam polarizers, broadband metamaterials, and antireflective solar cells.[16] Particularly, broadband transparent metal panels may play important roles in THz regime (10^{11} to 10^{13} Hz). It is known that the THz technology[17–21] is widely applied in information and communications technology (ICT), biology and medical sciences, homeland security, and so on. Our findings provide a novel design for transparent conducting panels with simultaneously desired electrical and optical performance, which may significantly benefit the ICT.

The one-dimensional metallic grating shown in **Figure 1**a is one of the simplest metallic structures, where d, W, and τ denote the grating period, the slit width, and the grating thickness, respectively. Using the rigorous coupled-wave analysis (RCWA)[22,23] and finite-difference time-domain (FDTD)[24] calculations, one can find that within a certain angular range of oblique incidence, the metallic grating can become transparent in the entire long wavelength regime for transverse magnetic (TM) polarization. For example, Figure 1b shows the calculated transmission through gold gratings with grazing incidence angle $\theta = 84°$. The gratings indeed become highly transparent for all wavelengths $\lambda > d\ (1 + \cos\theta) \approx 2d$. The unusual transparence phenomenon occurs within a certain angular range around $\theta = 84°$. Meanwhile, the top grating surfaces become completely anti-reflective. These results are surprising and counterintuitive. Particularly for $\lambda >> d$, one might think that the incident wave could not resolve the details of the slit structures and should only see a homogeneous opaque metal averagely diluted by the slit gaps.

At the microscopic level, however, the metallic grating has rich physics. As illustrated in Figure 1a, the incident electric

Dr. R.-H. Fan, Prof. R.-W. Peng, Dr. J. Li, Dr. Q. Hu, Prof. M. Wang
National Laboratory of Solid State Microstructures and Department of Physics
Nanjing University
Nanjing 210093, China
E-mail: rwpeng@nju.edu.cn; muwang@nju.edu.cn
Dr. X.-R. Huang
Advanced Photon Source
Argonne National Laboratory
Argonne, Illinois 60439, USA
E-mail: xiahuang@aps.anl.gov
Dr. Y. Liu, Prof. X. Zhang
NSF Nano-scale Science and Engineering Center (NSEC)
3112 Etcheverry Hall
University of California
Berkeley, California 94720, USA

DOI: 10.1002/adma.201104483

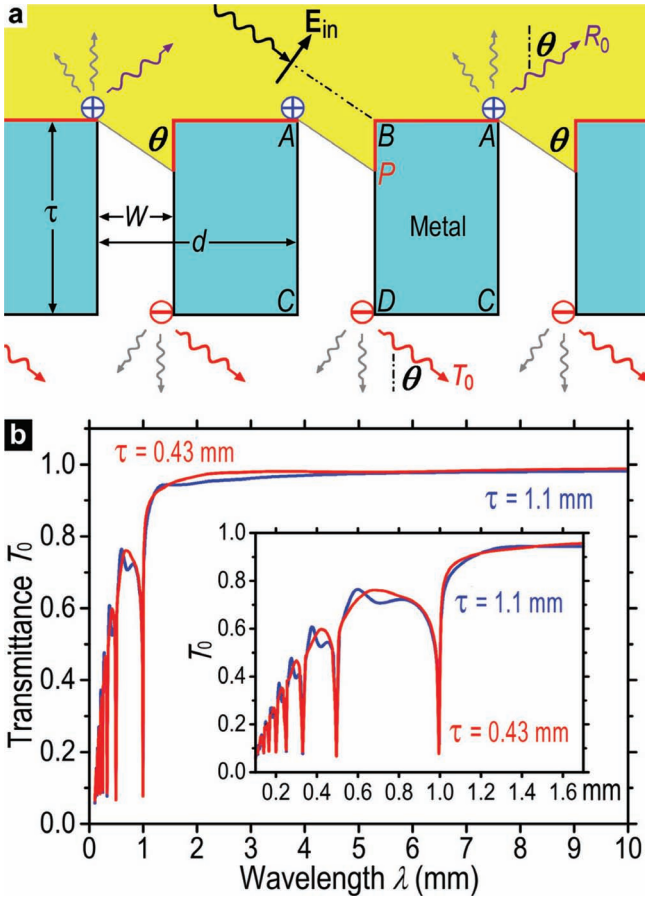

Figure 1. Light transmission through 1D metallic gratings with oblique incidence geometry. a) Schematic of light tunneling by moving electrons on the surfaces and slit walls. Note that for $\lambda > d(1 + \sin\theta)$, the scattered waves along directions other than the forward transmission (T_0) and specular reflection (R_0) directions are all evanescent (denoted by gray rays). b) Transmittance of TM-polarization light calculated for gold gratings with period $d = 0.5$ mm, slit width $W = 0.05$ mm, and thicknesses $\tau = 0.43$ and 1.1 mm, at $\theta_f = 84°$ as specified by equation (1). The inset shows the transmission variation in the shorter-wavelength range, where the sharp transmittance dips correspond to Wood anomalies satisfying $d(1 + \sin\theta) = n\lambda$ ($n = 1,2,3,\ldots$). TM polarization. Red and blue curves correspond to the cases of $\tau = 0.43$ mm and $\tau = 1.1$ mm, respectively.

field $\mathbf{E}_{in}\, e^{i\omega t}$ (ω is the circular frequency of the incident wave) illuminates both the top surface AB and part of the slit wall, BP, and drives free electrons there to move as surface charge density waves. These waves propagate continuously on the wall PD, but are stopped at corner D to form high-density charges that oscillate with $e^{i\omega t}$ and emit the transmitted wave (T_0). The transmission efficiency reaches the maximum at the incidence angle[6]

$$\theta_f \approx \arctan\,(d/W - 1) \tag{1}$$

Note that charge accumulation also occurs at corner A, from which the emitted wavelets offset the specularly reflected wavelets from surface AB to minimize the overall reflection.

To experimentally realize transparent metals, we have prepared different metallic gratings with varied geometries for transmission measurements in the THz frequency band, where the metals are highly conductive with negligible Ohmic loss. **Figure 2**a shows the optical image of one of the gold grating. The measurements are carried out with an Ekspla THz real-time spectrometer, as schematically shown in Figure 2b. The time-domain signal $E(t)$ of the polychromatic THz pulse transmitted through the grating with different incident angles θ are shown in Figure 2c. Obviously, the grating is partially transparent at all the incident angles, but the signal amplitude increases as θ is approaching 68°, indicating that the overall transmission efficiency of the grating increases at high incident angle for the incident THz pulse. It is known that the strongest and nearly flat white-beam transmission can occur only for $\lambda > \lambda_{WD1}$ with oblique incidence, and $\lambda_{WD1}(\theta) = d(1 + \sin\theta)$ is the wavelength where the first-order Wood anomaly occurs. Subtracting these shorter-wavelength contributions from the Fourier transform of the signals in Figure 2c, we obtained the average transmission efficiency (T_L) curves in Figure 2d for long wavelengths from 1.05 to 1.5 mm. Here T_L increases remarkably from 28% at $\theta = 0$ to 80% around $\theta = 68°$. The maximum transmission angle $\theta \sim 68°$ in fact agrees well with $\theta_f = 66.8°$ predicted by Equation (1) for the air void filling ratio $W/d = 0.3$.

The transmittance spectra $T_0(\lambda)$ obtained from Figure 2c by Fourier transformation are shown in Figure 2e. For comparison, we illustrate also in Figure 2e the corresponding spectra calculated by the RCWA method. These computations were also verified by FDTD calculations with a pulsed incident beam. The calculated maximum transmittance is nearly 100% due to the negligible Ohmic absorption of the grating. The measured maximum transmittance is, however, about 83%, which could be caused by the imperfections of the grating, such as the surface roughness and the fluctuation of the slit width. Despite of the attenuation of the strength, the major features of the measured spectra are in good agreement with the calculations (Figure 2e). The transmittance dip marked by the arrow corresponds to the first-order Wood anomaly at $\lambda_{WD1}(\theta) = d(1 + \sin\theta)$, which correctly shifts from d toward $2d$ by increasing θ. For normal incidence $\theta = 0°$, the transmission peaks are known as Fabry-Perot (FP) resonance peaks occurring at $\lambda_N = 2\tau/N + \Delta_N$, where $N > 0$ is an integer and Δ_N is the redshift of the peak.[4,25–27] Here for $\theta = 0°$, the second-order FP peak ($N = 2$) is partially truncated at λ_{WD1}. Beyond the FP resonance ranges, the transmission is very low (particularly for thick gratings).

For oblique incidence, Figure 2e shows that the long-wavelength transmission gradually increases as θ is increased. For $\theta = 68°$, the transmittance becomes nearly constant for $\lambda > \lambda_{WD1}$, with $T_0 \sim 83\%$ and 99% for the measurements and calculations, respectively. Our THz spectrometer only covers the wavelength range between 0.3 and 1.5mm, yet RCWA calculations show that the nearly flat transmission at $\theta = 68°$ in Figure 2e extends to the radar wave band, similar to the curves in Figure 1b. The flat T_0 curves have little change in the range $67° < \theta < 72°$. Limited by our experimental setup, we are not able to measure the transmission for $\theta > 75°$. So in the last panel of Figure 2e we only present the calculated transmission spectra for $\theta = 75°$, 80°, and 85°, from which one can see that the long-wavelength transmittance drops when $\theta > 75°$. Therefore, the angular range $67° < \theta < 75°$ is the maximum and nearly flat transmission range for the current grating, which is close to the prediction of Equation (1).

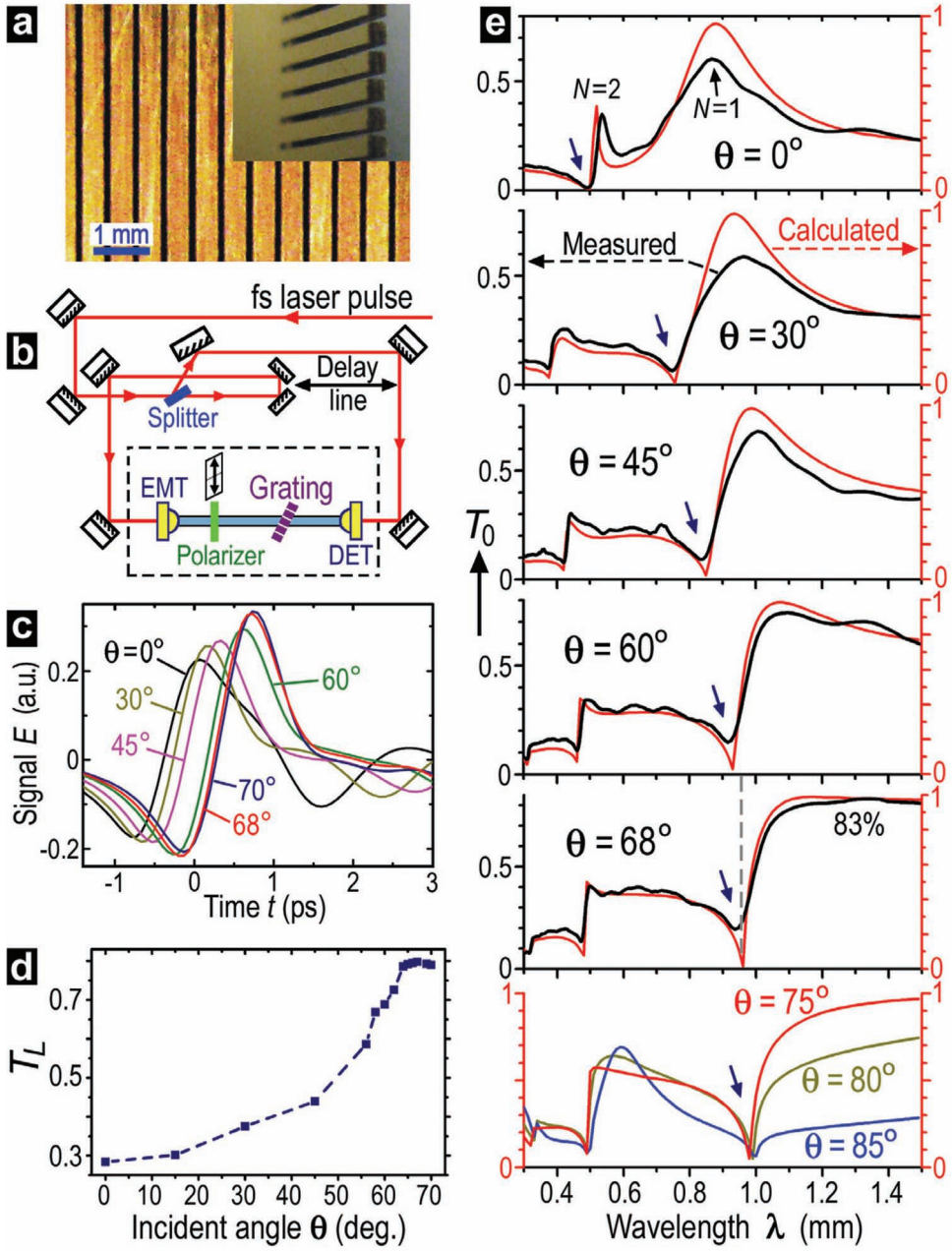

Figure 2. Measurements and calculations of TM-polarization light transmission through a gold grating. a) Optical image of the grating. The insert shows the cross section. $d = 0.5$ mm, $W = 0.15$ mm, and $\tau = 0.34$ mm. b) Schematic of the experiment setup. EMT: THz emitter. DET: THz detector. The dashed-line box is a nitrogen purging box. c) Time-domain THz transmission signals for different incident angles. d) Average transmission efficiency for 1.05 mm ≤ λ ≤ 1.5 mm. e) Comparison of the measured and calculated transmission spectra. Note that the regime where broadband flat transmission occurs is for the wavelengths larger than λ_{WD1} marked by black arrow.

By measuring the optical spectra of oblique incidence from $\theta = 0$ to $\theta = 72°$, we obtain the angular transmission spectra and the dispersion map of the gold grating shown in **Figures 3**a and Figure 3c, respectively. It is evident that the maximum transmission appears around $\theta = 68°$, as marked by the dashed lined in Figure 3a. Broadband high transparency indeed occurs in the range $67° < \theta < 72°$ (as shown in Figures 3a and 3c). Therefore, we confirm that metallic gratings become highly transparent for broadband long wavelengths with oblique incidence.

To verify further the broadband transparency of structured metals, we examine another grating with the same lattice parameter as previous one but with different thickness, τ = 0.22 mm. The measured angular transmission spectra and the dispersion map of this grating are illustrated in Figures. 3b and 3d, respectively. The maximum transmission still appears around $\theta = 68°$ (as marked in Figure 3b), and high broadband transparency is preserved (as shown in Figures 3b and 3d). Comparing with the first sample, here only the first-order FP

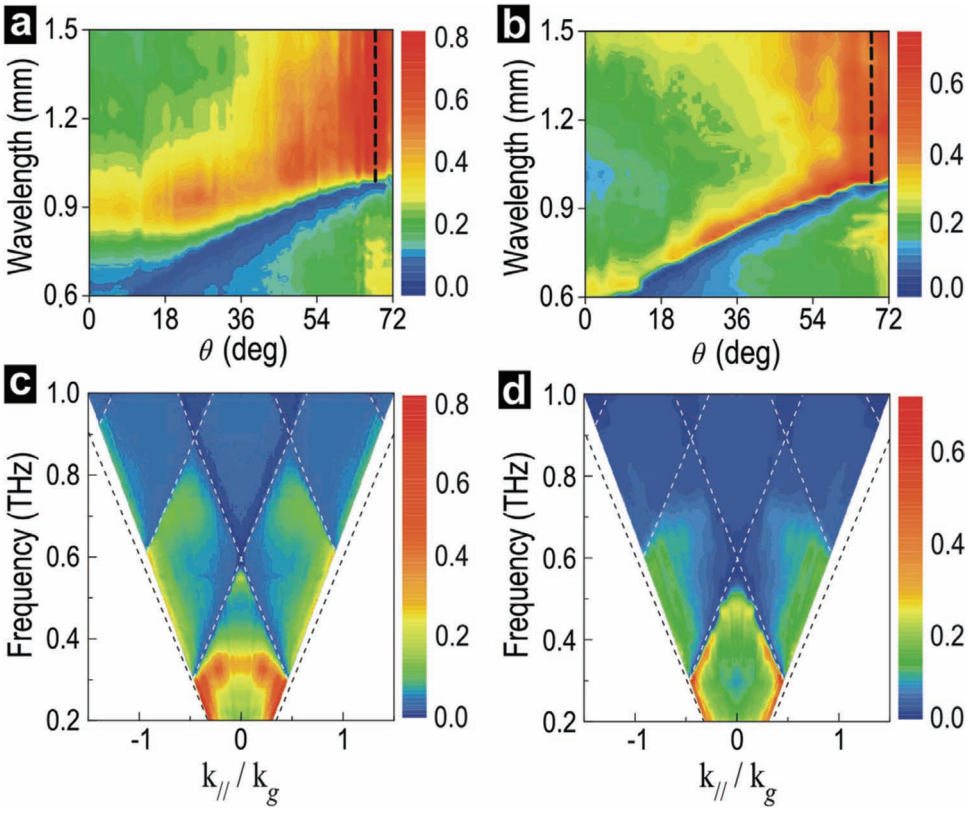

Figure 3. Experimentally measured angular transmission spectra of the gold gratings with period $d = 0.5$ mm, slit width $W = 0.15$ mm, but a different thickness(τ): a) $\tau = 0.34$ mm; b) $\tau = 0.22$ mm. The black dashed lines in (a) and (b) indicate the maximum transmission angles. Experimentally measured dispersion maps of the two gratings: c) $\tau = 0.34$ mm; d) $\tau = 0.22$ mm. Black dotted lines in (c) and (d) represent light cone lines, white dotted lines in (c) and (d) show the position of Wood anomaly. $k_{//} = 2\pi \sin\theta/\lambda$ is the in-plane wave vector, and $k_g = 2\pi/d$ is the reciprocal lattice vector. Here incident angle θ ranges from 0 degree to 72 degree. Color bar shows the measured transmission intensity.

peak appears for normal incidence, whereas all other FP peaks fall below λ_{WD1} (as shown in **Figure 4**a) because of the smaller thickness τ of the second sample. The T_0 curves for small incident angles θ are different from their counterparts in Figure 2e. However, the nearly flat transmission spectra of the two gratings at $\theta = 68°$ (to see Figure 4b and Figure 2e) are very similar in the long-wavelength range $\lambda > \lambda_{WD1}$. These experiments indicate that the broadband transmission is insensitive to the grating thickness τ, and it is irrelevant to the FP resonance that sensitively depends on the thickness. More examples are given in the Supporting Information.

The microscopic mechanism of light transmission through the slits with the assistance of free electron oscillation can be understood as follows. For the scenario of normal incidence and FP resonance, the charge distribution of the second grating at a specific time is calculated and shown in Figure 4c, where the charge densities at the four corners reach the maximum. Continuously temporal distributions of charge densities and electric fields for normal incidence can be found in Movie S1 in the Supporting Information. The incident electric field $\mathbf{E}_{in}$ drives the movement of free electrons on the top surface *AB*, and the electrons are trapped at corners *A* and *B* to form an oscillating dipole $\mathbf{P}_a$. $\mathbf{P}_a$ emits a wavelet inside the slit, which excites the free electrons on the slit walls and forms downward-propagating SPs. When the SPs reach the bottom, the charge movement is discontinuous at corners *C* and *D*, inducing another oscillating dipole $\mathbf{P}_b$. Thereafter, SPs are bounced backward to the upper surface to interfere with $\mathbf{P}_a$. Thus, $\mathbf{P}_a$ and $\mathbf{P}_b$ eventually form FP resonance under the condition $N\lambda \approx 2\tau$, where $N > 0$ is an integer and λ is the wavelength of the incident light.[6] The wavelets emitted from the periodic dipoles $\mathbf{P}_b$ along the forward direction form the transmitted beam. In the scenario that FP resonance condition is not satisfied, $\mathbf{P}_a$ and $\mathbf{P}_b$ interact destructively, hence no strong transmission takes place.[25] The FP resonance makes it possible to use the grating as a wire grid polarizer,[28] but such effects depend on the grating thickness.

For the oblique incidence, as illustrated in Figure 1a, the incident beam directly illuminates part of the slit wall (*BP*), thus applies a vertical driving force $e\mathbf{E}_w$ on the electrons on the slit wall (e denotes the charge per electron) that can significantly facilitate electron movement (i.e., propagation of SPs) on the walls. In particular, when the total forces exerted on *AB* and *BP* are balanced, the electrons can move smoothly around corner *B* without charge accumulation. Then the charge waves formed on *AB* and *BP* may propagate continuously on the unilluminated wall *PD* to the bottom. With this balanced-force condition, the tendency for SPs to be bounced back is almost completely suppressed by the force $e\mathbf{E}_w$. Subsequently, the FP resonance does not occur at the optimal incidence angle θ_f and the electrons move continuously on the entire surfaces *AB* and *BD*, resulting

ADVANCED MATERIALS
www.advmat.de

www.MaterialsViews.com

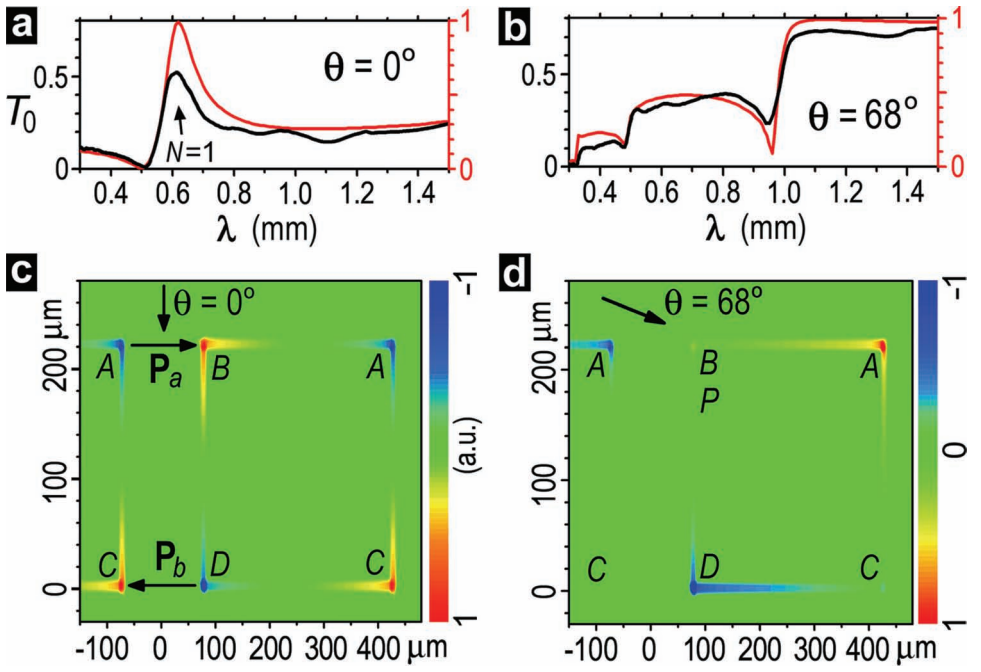

Figure 4. Measurements and calculations of TM-polarization light transmission through the gold grating: a) $\theta = 0°$; b) $\theta = 68°$. Instantaneous charge distribution calculated at: c) $\lambda = 0.62$ mm and $\theta = 0°$; d) $\lambda = 1.2$ mm and $\theta = 68°$. In the grating, $d = 0.5$ mm, $W = 0.15$ mm, and $\tau = 0.22$ mm.

in strong light transmission through the slits (see Ref. 6). In the THz band, this picture is exactly verified by the charge distribution in Figure 4d, where high charge accumulation does occur at corners *A* and *D* but is nearly absent at corner *B* under the balanced-force condition. The emission of the transmitted light from the charge oscillation is illustrated more clearly by temporal distributions of charge densities and electric fields in Movie S2 of the Supporting Information. Therefore, we suggest that SP excitation occurs only on the active surface *AB* and *BP*. Once the SP is excited in the balanced-force condition, the SPs can freely propagate on the slit wall *PD* towards the bottom if the Ohmic loss of the metals is negligible. This explains why the flat transmission process is insensitive to the grating thickness, as demonstrated above. Thus, broadband extraordinary transmission can occur through extremely thick gratings. For instance, our calculations show that the nearly flat transmittance T_0 remains above 70% when $\tau = 10$ cm (about 100 times larger than the wavelength) and $W/d = 0.3$ in the THz band.

As indicated by Equation (1), the optimal incidence angle θ_f for broadband transparence strongly depends on the air void filling ratio W/d. In our experiments, this has been verified from gratings with different ratios W/d (see the Supporting Information). As another example, **Figure 5**a shows the calculated flat transmittance spectrum of a thick gold grating with a small ratio $W/d = 0.05$, where the optimal incident angle $\theta_f = 87°$ obtained from RCWA calculations satisfies Equation (1) quite well. Comparing with the normal-incidence spectrum, the extraordinary transmission (>90%) is remarkable in terms of the extremely narrow slits (compared with d and λ) and the large thickness $\tau = 2.5$ mm.

Figure 5b shows the dependence of θ_f on the ratio W/d calculated from Equation (1) and RCWA, respectively. In general, the curves show that θ_f decreases with increasing W/d, which is consistent with our experiments. For $W/d \leq 0.1$, the results from Equation (1) and RCWA are in agreement near perfectly,

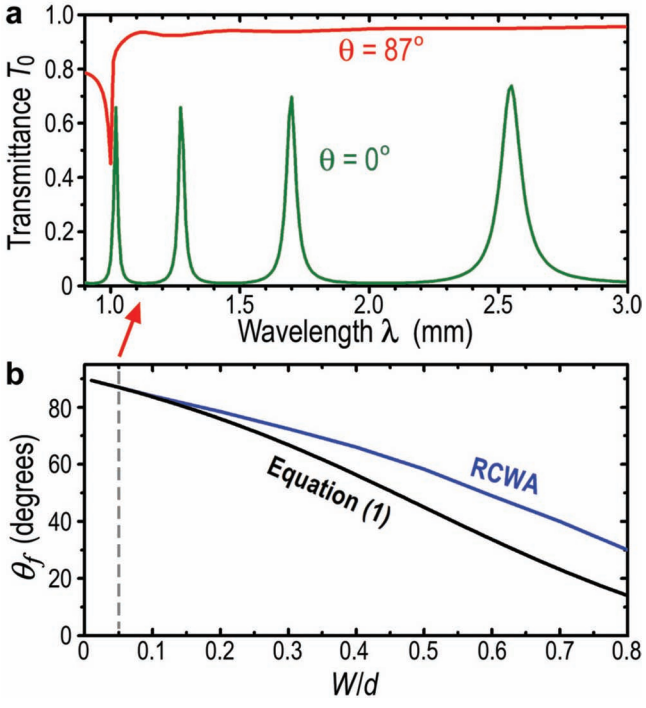

Figure 5. Dependence of the optimal flat transmission angle θ_f on the ratio W/d. a) Comparison between the flat transmittance curve at $\theta_f = 87°$ and the normal-incidence transmittance curve. $W = 25$ μm, $d = 0.5$ mm, $\tau = 2.5$ mm. b) Dependence of θ_f on W/d calculated by RCWA and Equation (1). Note that these two curves are almost completely independent of the grating thickness τ.

as illustrated in Figure 5a and Figure 1b as examples. But for large W/d, θ_f predicted by Equation (1) is generally smaller than that from RCWA calculations. However, note that for each W/d, the nearly flat transmission can occur within a finite incident angular range (from ~1° for $W/d \leq 0.1$ to ~10° for $W/d > 0.5$). In Figure 5b, each point on the θ_f curve obtained from RCWA represents the center of this angular range. Taking this fact into account, one may see that the discrepancies between the two curves are not significant. Therefore, although Equation (1) is not always rigorous, it still captures the microscopic mechanism underlying the broadband transparence phenomenon.

With the assistance of surface plasmons, metallic gratings become non-dispersively transparent to broadband electromagnetic waves for oblique incidence. However, the oblique-incidence geometry illustrated above may be inconvenient for technological applications, as mentioned by Subramania et al. in Ref. 8. To solve this problem, an alternative approach is to use the oblique grating illustrated in **Figure 6**a to achieve broadband transparency under normal incidence. Based on the force-balance condition,[6] the optimal oblique angle of the grating can be achieved as follows. The total force applied on the upper surface by the incident electric field $\mathbf{E}_{in}$ can be expressed as $F_u = (eE_{in}\cos\varphi)\, aI_u$, where $I_u \propto \cos\varphi$ is the effective photon density incident on the surface BA. The total force exerted on the illuminated slit wall BP is $F_w = (eE_{in}\sin\varphi)l_w I_w$, where $l_w = [(d/\cos\varphi) - a\cos\varphi)]/\sin\varphi$ is the length of the illuminated wall BP and $I_u \propto \sin\varphi$ is the photon density incident on the wall. The balanced-force condition requires $F_u = F_w$. It follows that the optimal oblique angle φ_f should obey

$$a(1+\tan\phi_f)/(1+\tan^2\phi_f) = d\tan\phi_f \quad (2)$$

For an oblique grating with lattice parameters $a = 0.3$ mm and $d = 0.56$ mm, Equation (2) predicts $\varphi_f = 32°$ for broadband high transmission with normal incidence.

To verify the transparent of oblique gratings under normal incidence, we fabricated two thick gratings with the lattice parameters $a = 0.3$ mm and $d = 0.56$ mm, one with an oblique angle of $\varphi = 32°$ and the other with $\varphi = 0$ (regular grating), as shown in Figures. 6b and 6c, respectively. Figures 6d and 6e show the experimentally measured normal-incidence ($\theta = 0°$) transmission spectra and the corresponding FDTD calculations of these two gratings, respectively. Apparently, the spectra of the two gratings are quite different from each other although the gratings have the same effective ratio $W/d = 0.464$. Note that the horizontal period of the oblique grating becomes $d/\cos\varphi = 0.66$ mm. Consequently, the first-order Wood anomaly shifts to $\lambda_{WD1} = 0.66$ mm from 0.56 mm for the regular grating. Comparing with that of the regular grating, the FP effect of the oblique grating is significantly suppressed above λ_{WD1}. Therefore, the average transmission efficiency in the long-wavelength range $\lambda > \lambda_{WD1}$ is much higher than that of the regular grating. In particular, the transmittance tends to be flat in the range 0.7 mm < λ < 1.0 mm in Figure 5d with the maximum transmittance close to 100% (for $\tau = 1.95$ mm), despite that the FP effect is not completely suppressed for $\lambda > 1$ mm. Therefore by tuning the ratio W/d and the φ angle of the oblique grating, high broadband transmittance can be realized for normal incidence.

In conclusion, we have demonstrated in this communication that metallic gratings with narrow slits can become highly transparent for extremely broad bandwidths with oblique incidence or with normal incidence for oblique gratings. The broadband optical transmission is verified for the structured metals with thickness within the range of half a wavelength, and the high transmission efficiency is insensitive to the metal thickness. In particular, thick metal gratings possess both advantages of extremely high-efficiency transmission and high-performance electrical properties, which may have many potential applications in information and communications technology and other fields. Currently the experiments are carried out in THz band, yet continuous and nearly unitary transmission can be achieved in the broadband frequency ranging from visible light to radio wave. Our observations demonstrate a simple yet efficient way to make broadband transparent metals, based on which more complicated applications on antireflection solar cells and stealth technologies, for example, can be anticipated. The physics underlying the shown phenomena may also shed new light on widening the bandwidths and increasing of the efficiency of more complicated structured materials, including sonic artificial materials.

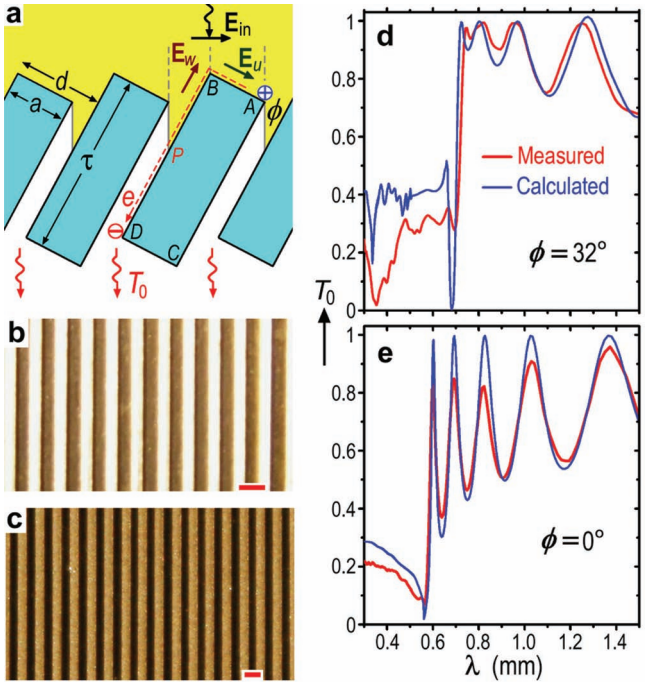

Figure 6. Comparison between transmission through oblique and regular gratings under normal incidence. a) Schematic of the oblique grating. b,c) Top-view optical micrographs of the oblique ($\phi = 32°$) and regular ($\phi = 0°$) gratings, respectively. $d = 0.56$ mm, $a = 0.3$ mm, and $\tau = 1.95$ mm. The top-view period (red scale bar) of the oblique grating in (b) is $d/\cos\phi = 0.66$ mm while in (c) the period is 0.56 mm. d,e) Measured and calculated normal-incidence transmission spectra of the two gratings.

Experimental Section

Fabrication Methods for the Structures: The grating patterns are designed by the software (AutoCAD, 2007), and transferred onto both sides of an aluminum plate via photochemical reaction. The uncoated

parts of the aluminum plate are then removed by chemical etching on both sides in order to construct normal gratings. Finally, to protect aluminum plates and enhance the conductivity of the grating surface, 3 μm-thick gold films are coated on all the surfaces (including the slit walls) by magnetron sputtering. The oblique grating is assembled with metallic strips. The metallic strips are first achieved by cutting the normal gratings. Then, the strips are fixed at the desired angle ($\varphi = 32°$) with certain period.

Optical and Structure Characterization: The measurements are carried out with an terahertz (THz) real-time spectrometer (EKSPLA/THz, Lithuania), where the femtosecond pulsed laser beam is split by a 50:50 splitter into two beams, one as the reference beam and the other directed along an optical delay line. The latter then illuminates the THz emitter to produce the THz pulse, which is TM polarized before the grating. The emitter and detector are two photoconductor antennas. By scanning the delay line, we obtain the time-domain signal $E(t)$ of the polychromatic THz pulse transmitted through the grating with respect to the reference laser pulse. Afterwards, the transmission spectrum is obtained from the Fourier transform of $E(t)$ for λ from 0.3 to 1.5 mm, and the measured spectra are normalized with respect to the transmittance spectra of air. Carrying out fine measurements of the optical spectra at oblique incidence from $\theta = 0$ to $\theta = 72°$ with steps of 1°, we experimentally obtain the angular transmission spectra and the dispersion map of the gold grating.

Supporting Information

Supporting Information is available from the Wiley Online Library or from the author.

Acknowledgements

This work was supported by the Ministry of Science and Technology of China (Grant Nos. 2012CB921502 and 2010CB630705), the National Science Foundation of China (Grant Nos. 11034005, 61077023, 10874068 and 11021403), and partly by Jiangsu Province, China (BK2008012). X.-R.H. was supported by the Advanced Photon Source, an Office of Science user facility operated for the U.S. Department of Energy (DOE) Office of Science by Argonne National Laboratory and supported by the U.S. DOE under Contract No. DE-AC02-06CH11357.

Received: November 23, 2011
Revised: January 22, 2012
Published online: March 19, 2012

[1] W. L. Barnes, A. Dereux, T. W. Ebbesen, *Nature* **2003**, *424*, 824.
[2] J. B. Pendry, L. Martin-Moreno, F. J. Garcia-Vidal, *Science* **2004**, *305*, 847.
[3] T. W. Ebbesen, H. J. Lezec, H. F. Ghaemi, T. Thio, P. A. Wolff, *Nature* **1998**, *391*, 667.
[4] J. A. Porto, F. J. García-Vidal, J. B. Pendry, *Phys. Rev. Lett.* **1999**, *83*, 2845.
[5] H. Liu, P. Lalanne, *Nature* **2008**, *452*, 728.
[6] X. R. Huang, R. W. Peng, R. H. Fan, *Phys. Rev. Lett.* **2010**, *105*, 243901.
[7] A. Alù, G. D'Aguanno, N. Mattiucci, M. J. Bloemer, *Phys. Rev. Lett.* **2011**, *106*, 123902.
[8] G. Subramania, S. Foteinopoulou, I. Brener, *Phys. Rev. Lett.* **2011**, *107*, 163902.
[9] I. R. Hooper, T. W. Preist, J. R. Sambles, *Phys. Rev. Lett.* **2006**, *97*, 053902.
[10] Y. J. Bao, R. W. Peng, D. J. Shu, Mu Wang, X. Lu, J. Shao, W. Lu, N. B. Ming, *Phys. Rev. Lett.* **2008**, *101*, 087401.
[11] N. Liu, L. Fu, S. Kaiser, H. Schweizer, H. Giessen, *Adv. Mater.* **2008**, *20*, 3859.
[12] Y. M. Liu, X. Zhang, *Chem. Soc. Rev*. **2011**, *40*, 2494.
[13] N. Fang, H. Lee, C. Sun, X. Zhang, *Science* **2005**, *308*, 534.
[14] R. A. Shelby, D. R. Smith, S. Schultz, *Science* **2001**, *292*, 77.
[15] J. T. Shen, P. B. Catrysse, S. Fan, *Phys. Rev. Lett.* **2005**, *94*, 197401.
[16] H. A. Atwater, A. Polman, *Nat. Mater.* **2010**, *9*, 205.
[17] P. H. Siegel, *IEEE Trans. Microwave Theory Tech.* **2002**, *50*, 910.
[18] B. Ferguson, X. C. Zhang, *Nat. Mater.* **2002**, *1*, 26.
[19] M. Tonouchi, *Nat. Photon.* **2007**, *1*, 97.
[20] J. Lott, C. Xia, L. Kosnosky, C. Weder, J. Shan, *Adv. Mater.* **2008**, *20*, 3649.
[21] J. F. O'Hara, R. Singh, I. Brener, E. Smirnova, J. Han, A. J. Taylor, W. Zhang, *Opt. Express* **2008**, *16*, 1786.
[22] P. Lalanne, G. M. Morris, *J. Opt. Soc. Am. A* **1996**, *13*, 779.
[23] B. Guizal, H. Yala, D. Felbacq, *Opt. Lett.* **2009**, *34*, 2790.
[24] A. Taflove, S. C. Hagness, *Computational Electrodynamics: The Finite-Difference Time-Domain Method*, 3rd ed., Artech House, Norwood, **2005**.
[25] X. R. Huang, R. W. Peng, *J. Opt. Soc. Am. A* **2010**, *27*, 718.
[26] H. E. Went, A. P. Hibbins, J. R. Sambles, C. R. Lawrence, A. P. Crick, *Appl. Phys. Lett.* **2000**, *77*, 2789.
[27] S. Collin, G. Vincent, R. Haïdar, N. Bardou, S. Rommeluère, J. L. Pelouard, *Phys. Rev. Lett.* **2010**, *104*, 027401.
[28] P. Yeh, *Opt. Commun.* **1978**, *26*, 289.